



Geomagnetically Induced Current Analyzed with Wavelet Extraction

Odim Mendes¹  · Kai Schneider²  · Margarete Oliveira Domingues¹  · Marie Farge³  · Nalin Babulal Trivedi¹ · Peter Frick⁴  · Natacha Nguyen van yen³

Received: 28 March 2022 / Accepted: 28 July 2022

© The Author(s) under exclusive licence to Sociedade Brasileira de Física 2022

Abstract

Investigation of electrodynamic effects considering South American features is essential to extend understanding of middle- to low-latitude space weather phenomena. For retrieving magnetic contributions related to geomagnetically induced currents (GIC), a wavelet-based filtering method is verified and applied to magnetic records on the ground. The experimental data with one-minute resolution were acquired with magnetometers at two Brazilian sites, close to the South Atlantic Magnetic Anomaly, from Nov. 6 to 11, 2004. The signal intensities vary primarily under the influence of the geomagnetic disturbance periods. The performed wavelet analyses allow for a scale-dependent statistical characterization (including their cross-correlation) of the magnetospheric-ionospheric processes that affect the Earth's surface. The non-stationary magnetic signals can thus be split into coherent events and background noise by the wavelet denoising technique. The statistics and physical features of both parts are analyzed, and it is shown that the proposed treatment yields a deperated GIC signal. As a complementary result, this procedure also establishes an objective-automatic computational method for the GIC calculation treatment.

Keywords Geomagnetically induced current · Wavelet analysis · Space electrodynamics · Space weather

Kai Schneider, Margarete Oliveira Domingues, Marie Farge, Nalin Babulal Trivedi, Peter Frick and Natacha Nguyen van yen contributed equally to this work.

Nalin Babulal Trivedi died before publication of this work was completed.

This article is dedicated to the memory of Nalin Babulal Trivedi.

✉ Odim Mendes
odim.mendes@inpe.br

Kai Schneider
kai.schneider@univ-amu.fr

Margarete Oliveira Domingues
margarete.domingues@inpe.br

Marie Farge
marie.farge@ens.fr

Peter Frick
frick@icmm.ru

Natacha Nguyen van yen
romain.nguyenvanyen@gmail.com

1 Introduction

Disturbances of the regular dipolar magnetic field near the Earth's surface are consequences of complex electrical current systems surrounding the planet and, to some extent, of currents inside the Earth itself [1–3]. Magnetograms recorded on the surface may include, in addition, magnetic disturbances caused by industrial sources. Although the results of those last sources are usually considered as noise in geophysical observations, they do allow the detection of some localized features of the geomagnetic field. For

¹ INPE, Av. dos Astronautas, São José dos Campos 12227-010, São Paulo, Brazil

² Institut de Mathématiques de Marseille (I2M), CNRS, Aix-Marseille Université, 39 rue F. Joliot-Curie, 13453 Marseille cedex 13, France

³ LMD-CNRS, Ecole Normale Supérieure-PSL, 24 rue Lhomond, 75321 Paris cedex 05, France

⁴ Institute of Continuous Media Mechanics, Ural Branch of the Russian Academy of Sciences, Korolyov str. 1, Perm 614018, Russia

example, the presence of an electrical transmission line can be used to reveal the magnetic field induced by large-scale natural currents parallel to this line [4]. Indeed, examining magnetic records from two different stations which are close in the geophysical sense, i.e., less than few hundred kilometers, with one being localized in the vicinity of transmission lines and the other far away, one can extract the contribution of natural currents parallel to this line.

For space weather effect investigation [5], many studies have been developed since the end of the last century. They analyze the interaction between the interplanetary causes and electrodynamics occurring in the Earth [6]. The higher latitude regions are exposed naturally to those kinds of external influences. Notably, dealing with the Geomagnetically Induced Currents (GIC) at Northern region (above 40° of geomagnetic latitude), Pulkkinen and team [7] presented a 100 year of survey results concerning those manifestations. Falayi and team [8] presented an exciting investigation on the GIC behavior at high latitude during storm-time variations, highlighting rich processes.

Since then, much more work has been developed about the theme, mainly pointing out the importance of the effects on middle and low latitudes [9, 10]. Relevant aspects have been deserved attention, such as the existence of long-extension electrical-energy transmission grids [10]. Once even for low GIC intensities, transients affect transformers and produce deleterious consequences [9]. Additionally, several studies have explored the subject in terms of qualified GIC models for extended sensor networks [11], GIC modelling for transmission grids [12, 13], mainly modelling analysis dealing with peculiarities for GIC occurrences [14].

To comprehensively understand GIC formalisms, someone can consult Pirjola's work [15], where he elegantly explained their fundamentals, highlighting inclusive practical uses. In the context of middle- to low-latitude events, the GIC occurrences are affected by a complex electrodynamics scenario in the South American Region, as the case dealt here Beyond the noise from human sources, several significant phenomena contribute like the South Atlantic Magnetic Anomaly (SAMA), the equatorial ionospheric electrojet, the equatorial plasma vertical drift (fountain effect), the highest magnetic equator tilt concerning the geographical equator, and the most extensive territorial extension grids crossing the region [16]. Currently, varieties of investigations have added contributions to the GIC understanding at lower latitudes, at the same time in an electrodynamically complicated region, such as the work developed by Barbosa and team [17], Alves and team [18] and Espinosa and team [19].

Based on a significant work at the Brazilian region [2, 20], our conceptual examination aims to verify the white noise interference on ground geomagnetic measurements, which are used in the GIC studies, as discussed by Pirjola et al. [15]. We select a treatment methodology that deals with data

under non-stationary regimes and obeys non-linear processes, the wavelet transform technique [21]. In this paper, we analyze data from magnetometers at the Vassouras observatory (abbreviated as VSS), Rio de Janeiro, Brazil, and from a device installed under a transmission line (TL) at an experimental site in Pimenta-Barreiro (PIM), Minas Gerais, Brazil, in order to record the effects of GICs. The goal of this paper is to extract the GIC contribution even under conditions in which the signals from both stations exhibit a non-trivial, non-stationary behavior.

We start with a wavelet-based scale-by-scale cross-correlation analysis of both signals to deal with this task. Then we apply a wavelet-based method to split each signal into coherent and incoherent contributions, following the same approach as developed in [22] to study the time evolution of ion saturation current fluctuations in tokamaks. For a review on wavelet current fluctuations and their applications to MHD and plasma turbulence we refer to [23]. Initially, we evaluate if the geomagnetic measurements fulfil the statistical behavior to be subjected to the same treatment. The wavelet representation, in contrast to Fourier representation, does not require any hypotheses on the statistical stationarity, homogeneity and non-intermittency of the process under study. Thus, no a priori assumptions about the magnetosphere-ionosphere electrical current process and its effects on the Earth's surface have to be made. Furthermore, filtering methods based on the orthogonal wavelet transform are highly efficient for denoising signals corrupted with additive Gaussian white noise [24].

The importance of this kind of study is that the noisy background in the Brazilian data is significantly higher than in the data from some northern countries. Although not presented, a comparison was made with the data provided gently, in private communication, by the Finnish researcher Dr Ari Viljanen. As an example of his work, we mention the investigation of GIC in natural gas pipeline [25]. At last comment, this kind of treatment can be applied to other geomagnetic-dependent parameters concerning GIC occurrences.

The remainder of the paper is organized as follows. In Sect. 2, the Earth's current system and its magnetic effects are presented concisely, followed by the dataset description and the GIC-extraction procedure. In Sect. 3, the wavelet-based extraction methodology is described and extended to be applied to extract the contribution of GIC events. Corresponding scale-dependent statistical tools are also recalled. In Sect. 4, the results are presented and discussed. Finally in Sect. 5 some conclusions are drawn.

2 Geophysical Phenomena, Dataset and GIC

In this section, the geomagnetic disturbances and related GIC events are presented. The experimental datasets to be analyzed are described and the magnetic contributions to the signals are detailed.

2.1 Geomagnetic Disturbances and GIC Events

Disturbances of the close Earth's dipolar magnetic field are caused by different primary currents such as the magnetopause current, the tail current, the ring current, the field-aligned currents and the ionospheric currents. Illustrations and details on how these currents can be decoupled from each other, based on the involved mechanisms and resulting effects, are given in [26].

In a simplified fashion the physical mechanisms can be described as follows. From the solar wind-magnetosphere electrodynamic coupling, an electrical current is generated and flows in all the magnetopause, which corresponds the boundary between Earth's magnetic field domain and the surrounding solar wind plasma [6]. Details could be found in [27, Chapter 8, particularly Figure 8.15]. A current flows in that external layer, known as the magnetopause current, which enhances the magnetic field inside and cancels out the magnetic field in the immediate interplanetary medium surrounding. Composed of two lobes, the tail region as an extension of the magnetopause supports in the lower lobes a geomagnetic field that points far from the Earth and in the upper one, the geomagnetic field toward the Earth. Obeying a principle of electrodynamics discontinuity, a *neutral sheet current* is formed between the lobes, also a *plasma sheet* is structured. Schematically as a double solenoid, the magnetopause current interlinks with the neutral sheet current, and the latter flows from the dusk to the dawn side through the plasma sheet. The plasma sheet is characterized by a plasma with higher temperature and density than the surrounding region. [16]. In a complementary view, the Earth's dipolar magnetic field presents closed lines, which allow the trapped particles (ions and electrons) to drift slowly back and forth through adjacent field lines, an effect known as magnetic mirroring. Under this condition, electrically charged particles can circle the globe counterclockwise (electrons) and clockwise (positive ions), and simultaneously those particles obey a convective-driven motion towards the Earth. Spatial variations of the geomagnetic field cause the opposite movements, which generate a worldwide equatorial electric current, *the ring current*. The known *geomagnetic storms*, which are mid-to low-latitude magnetic disturbances at the Earth's surface, are the result of the magnetic induction produced by this current [28]. At lower latitudes, the geomagnetic field becomes weaker by about 0.5–1% [29, 30] The closest strongly ionized part of the atmosphere, *ionosphere*, between approximately 1000 and 100 km, also carries an electric current, which also contributes to the magnetic records. This region is affected by the magnetosphere electrodynamic disturbance [16].

Finally, the geomagnetic variations at the surface of the Earth induce electric currents in the crust and mantle of the Earth [1, 26, 31]. Those currents depend upon the frequency of the geomagnetic variations and the distribution of

the conductivity inside the Earth. The GICs end up flowing through electrical power transmission systems, as a ground manifestation of the space weather processes. GICs are functions of various parameters including the rate of change (i.e., the time derivative) of the geomagnetic field, the electric resistivity of the Earth, together with the geometry and resistances of the power grid considered. Therefore, full understanding of GICs can be achieved only via a complete study of the chain of physical processes linked with space weather changes during geomagnetic storms, and also with the effects of the resulting geomagnetic variations on the solid Earth for a certain conductivity distribution. Some reports on a GIC campaign made during more severe disturbed geomagnetic conditions at low and equatorial latitudes pointed out that they were very likely associated with ring current intensification. For the purpose of GIC studies, as well as space weather, magnetic records obtained on the surface of the Earth in a well-characterized way are necessary.

Nevertheless, for a complete contextualization, one final aspect may have a place in the considerations. As known, dB/dt variations that drive GICs on the ground are more likely to occur at high latitudes due to sudden variations of the auroral electrojets. While at lower latitudes, the main contribution comes from the magnetopause current, which is mainly driven by large-scale compressions caused by interplanetary shocks [32–34]. As the experiment is located far from the magnetic equator, the contribution effect expected from the equatorial electrojet current seems insignificant or, at least, negligible. Beyond the numerical treatment proposed, a question also arises in this work: what is the electrodynamic mechanism more directly related to this case of low-latitude GIC in the South Atlantic Magnetic Anomaly? Is this mechanism in agreement with the earlier GIC research results?

2.2 Geomagnetic Dataset

This study uses a TL oriented nearly in the geomagnetic east-west direction. Geoelectric fields in this direction tend to have a statistically somewhat more significant amplitude than north-south fields. This way, this condition produces larger GICs in east-west oriented transmission lines. From the three-component fluxgate magnetometers constructed at INPE [35], the measurements of geomagnetic field variations were started in August 2004 and with data collected under the selected TL. Situated in the western region of the state of Minas Gerais, at Pimenta-Barreiro, this TL is approximately 300 km away from the magnetic observatory of Vassouras/RJ, which is under the effects of the South Atlantic Magnetic Anomaly [36]. This observatory can be used as a reference station for GIC investigations in Southeast Brazil. More details on the electrical device are in [2, 20] and the map of the transmission lines in [17].

As basis for this study, the magnetometer records for a representative period, i.e., a period with a GIC event, were selected [31, 37]. The data we analyze for each site consist in a total of $N = 2^{13} = 8192$ samples, acquired with a time resolution of 1 minute over nearly 6 days, from November 6th to 11th, 2004. Among the different ways to represent the components of the geomagnetic field, we choose the representation of the horizontal, vertical and declination components. We focus only on the horizontal component, because it is considered representative of the magnetic disturbance for mid- to low-latitude stations.

For convenience Fig. 1 presents the magnetic signal resulting from the difference between the horizontal component of the geomagnetic field and its time-average. It represents a vanishing time-average value for each dataset measured at Vassouras observatory (bottom panel) and under the transmission line at the experimental site of Pimenta-Barreiro (top panel). Clearly identified by the depression two geomagnetic storms can be seen: one around Nov. 8th and the other around Nov. 10th. The interplanetary conditions connected to the GIC are presented in Appendix.

2.3 Contributions to the Signals

In the following, the time series of the horizontal component of the geomagnetic field at the Vassouras observatory and at the Pimenta-Barreiro site are denoted $H_{VSS}(t)$ and $H_{PIM}(t)$, respectively, where t is the time. They can be decomposed in several magnetic contributions as follows [4]. First, we suppose that both include a common spatial part provided by the magnetic field from outer sources, followed by individual

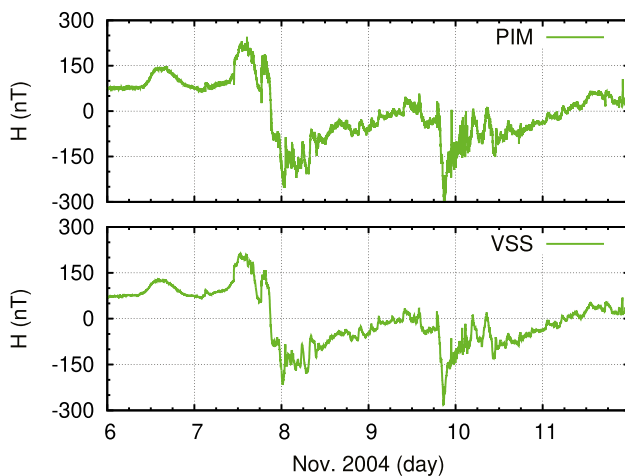


Fig. 1 Magnetic measurements at Vassouras observatory, Rio de Janeiro (bottom panel), and under a transmission line at Pimenta-Barreiro experimental site, Minas Gerais (top panel), Brazil, from Nov. 6th to 11th, 2004. For convenience for each dataset, the resultant signal of the horizontal component of the geomagnetic field subtracted by its mean value is presented

parts which include local features of the magnetic field, and also composed, at last, by a magnetic value of very slow time variation. Significantly, in addition, the signal $H_{PIM}(t)$, acquired close to the TL, includes a non-negligible contribution provided by a geomagnetically induced current, as consequence of the geoelectric field by Faraday's induction law. Our goal is then to extract this GIC contribution. In order to do that, we now describe the necessary wavelet-based tools.

3 Wavelet-Based Analysis Methodology

Different wavelet tools based either on the orthogonal or the continuous wavelet transform are applied to analyze the time series of the magnetic signals. The wavelet cross-correlation uses the continuous transform, while the orthogonal transform allows for an efficient denoising of the signals and the extraction of coherent events which yields the denoised GIC. Scale-dependent statistics further quantify the obtained results. For more complete details on wavelet transforms, the interested reader may consult textbooks, e.g., [21, 38].

3.1 Orthogonal Wavelets

Similar to classical spectral analysis which uses either the continuous or the discrete Fourier transform, for wavelet representations either the continuous or the discrete decomposition can be introduced, see, e.g., [38].

The discrete transform is based on the mathematical concept of multiresolution analysis, which considers approximations of the signal at different scales [21]. The resulting orthogonal wavelet bases allow a representation of the signal at large scales plus a sum of details when going to finer scales. The associated discrete filters yield a fast pyramidal numerical algorithm, which is known as the fast wavelet transform.

The orthogonal wavelet representation in the discrete setting (see, e.g., [22]), decomposes a function or a signal (i.e., a sampled function) into a set of embedded coarser and coarser approximations. The wavelet representation encodes the differences between successive finer approximations, corresponding to the wavelet coefficients, instead of the approximations themselves.

The wavelet coefficients contain the amount of information necessary to go from a coarse approximation to a finer approximation. The function, or the signal, can thus be represented by its coarsest scale approximation, and the corresponding scaling coefficients, plus the differences between the successive finer approximations, encoded by the wavelet coefficients.

In the following we consider a signal $S(t)$ of duration T which is sampled at equidistant instants $t_i = iT/N$, with $i = 0, \dots, N - 1$, where $N = 2^J$. The signal is then projected onto orthogonal wavelets and can be represented at different instants t_i and different time scales $\tau = 2^{-j}$, with $j = 0, \dots, J - 1$.

To this end we develop the signal into an orthogonal wavelet series,

$$S(t) = \bar{S}_{00}\phi_{00}(t) + \sum_{(j,i) \in \Lambda_J} \tilde{S}_{ji} \psi_{ji}(t) \tag{1}$$

where ϕ_{00} is the scaling function and ψ_{ji} the corresponding wavelets. The indices j, i correspond to the time scale $\tau = 2^{-j}$ and the time instant $t_i = i/2^j$. We introduce the index set Λ_J , defined as

$$\Lambda_J = \{(j, i), j = 0, \dots, J - 1, i = 0, \dots, 2^j - 1\}. \tag{2}$$

which indexes all wavelets of the basis in a concise way. The orthogonality of the wavelet basis implies that the coefficients can be computed using the L^2 inner product, $\langle \cdot, \cdot \rangle$. For the scaling coefficients we have $\bar{S}_{00} = \langle S, \phi_{00} \rangle$ and the wavelet coefficients are given by $\tilde{S}_{ji} = \langle S, \psi_{ji} \rangle$. As mentioned above the scaling coefficients encode the approximation of S at the largest scale $\tau_0 = 2^0 = 1$ and thus correspond to the mean value. The wavelet coefficients correspond to differences between approximations at two different time scales and yield the details necessary to get the finer time resolution. The Coifman 12 wavelets used here, have 4 vanishing moments and are almost symmetric. Two discrete filters, a low-pass and a band-pass filter, each with 12 filter coefficients [21] generate all functions of the wavelet basis. The scaling function $\phi(t)$ is defined by the low-pass filter, while the corresponding wavelet $\psi(t)$ is defined by the band-pass filter.

3.2 Denoising Using Orthogonal Wavelets

In [39] a wavelet-based method was proposed to split a signal $S(t)$ into two orthogonal components, coherent and incoherent signal contributions. While the coherent signal $S^C(t)$ contains the coherent events, the incoherent signal $S^I(t)$ is noise like and corresponds to the turbulent background fluctuations. To this end the signal $S(t)$ is projected onto an orthogonal wavelet basis. Then a threshold value ϵ is computed and the wavelet coefficients \tilde{S}_{ij} are separated into two sets: Coefficient with modulus larger than the threshold value ϵ , denoted as coherent coefficients \tilde{S}_{ij}^C and the remaining weak coefficients denoted as incoherent coefficients \tilde{S}_{ij}^I . Using the inverse wavelet transform the coherent signal component is reconstructed in physical space and we get $S^C(t)$. The incoherent component is obtained by pointwise subtraction $S^I(t) = S(t) - S^C(t)$. This yields the same result as applying the inverse wavelet transform to \tilde{S}_{ij}^I . The choice of the threshold is based on the assumption that the incoherent noise-like part is uncorrelated and has a normal distribution. This means we suppose that the signal contains additive Gaussian white noise. In this case the optimal threshold value is given by

$$\epsilon_D = (2\sigma^2 \ln N)^{1/2}. \tag{3}$$

where the variance of the noise σ^2 is known a priori. Using the wavelet representation this threshold, frequently called Donoho's threshold ϵ_D , was proven to be optimal for denoising signals in the presence of additive Gaussian white noise [24]. The authors have shown that the wavelet-based estimator minimizes the maximal L^2 -error (between the denoised signal and the noise-free signal) for functions with inhomogeneous regularity, such as intermittent signals. To determine the threshold ϵ_D the variance of the noise has to be known a priori. However, in most practical applications this is not the case and the variance needs to be estimated. To this end in [40] a recursive algorithm to estimate the variance of the noise has been proposed. Moreover the convergence of this iterative algorithm was proved for signals having sufficiently sparse representation in wavelet space, which is the case for intermittent signals.

The above wavelet thresholding yields a decomposition of the signal into $S(t) = S^C(t) + S^I(t)$. The orthogonality of the wavelets implies that the variance is split into $\sigma^2 = \sigma_C^2 + \sigma_I^2$, since the cross terms vanish, i.e., $\langle S^C, S^I \rangle = 0$.

3.3 Scale-Dependent Statistics

Scale-dependent statistics based on the wavelet representation of the signals yield further insights into their physical features. Using second-order statistics the wavelet spectrum can be defined which describes the scale distribution of the variance (or energy of the signal), similar to the Fourier spectrum. In addition to the Fourier spectrum the temporal localization of the wavelet basis allows a characterization of the temporal fluctuations of the variance using fourth-order moments, which is related to the scale-dependent flatness. For Gaussian signals the flatness has a value of three. Intermittent signals typically exhibit a departure from Gaussianity which can thus be quantified with the scale-dependent flatness. Finally, the probability density function (PDF) estimated using a histogram with adequate bins, quantifies higher order statistics of the signals.

3.3.1 The Fourier and Wavelet Spectrum

Information on the spectral distribution of energy from the magnetic signal can be obtained using either the Fourier spectrum or the wavelet spectrum, see, e.g., [22]. The classical Fourier spectrum is defined by:

$$E(\omega) = \frac{1}{2} |\hat{S}(\omega)|^2, \tag{4}$$

where $\hat{S}(\omega)$ denotes the Fourier transform, which is given by

$$\widehat{S}(\omega) = \int_{-\infty}^{\infty} S(t) e^{-i2\pi\omega t} dt \quad (5)$$

with $\iota = \sqrt{-1}$ and where ω denotes the frequency. Typically the periodogram which is the discrete version of Eq. 4, is used as an estimator for the spectrum. It is known to be a non consistent estimator due to the presence of oscillations [41], i.e., applying a periodogram to Gaussian white noise and increasing the sampling size does not yield a stabilized flat spectrum. Hence modifications are necessary to make it statistically consistent. For instance a modified periodogram can be computed by first tapering the data with a raised cosine window (affecting here 40 data points at each boundary) and then convolving the periodogram with a Gaussian window (with standard deviation of 40 data points). This modified periodogram yields a stabilized estimator of the spectrum, with no more oscillations, as discussed in [22]. Using the wavelet representation of the signal, given in Eq. 1, the scale distribution of the variance of the signal can be defined. This so-called scalogram [22], is given by

$$\widetilde{E}_j = \frac{1}{2} \sum_{i=0}^{2^j-1} |\widetilde{S}_{ji}|^2 \quad (6)$$

Summing over all scale contributions yields the total energy, $E = \sum_{j \geq 0} \widetilde{E}_j$, which is due to Parseval’s theorem. The frequency ω can be related to the scale index j using the relation $\omega_j = \frac{\omega_\psi}{2^j}$. The wavelet spectrum can be then defined as $\widetilde{E}(\omega_j) = \widetilde{E}_j / \omega_\psi$. Here ω_ψ is the centroid frequency of the mother wavelet. For the Coifman 12 wavelet the value is $\omega_\psi = 0.77$. The wavelet spectrum is a smoothed version of the Fourier spectrum (Eq. 4). The smoothing kernel corresponds to the modulus square of the Fourier transform of the wavelet [22]. For increasing frequency, i.e., when one goes to smaller scale, we observe that the smoothing interval becomes larger. This explains why the wavelet spectrum yields a consistent and well-conditioned statistical estimator of the spectrum. An advantage in comparison to the modified periodogram is that the smoothing window of the wavelet spectrum is automatically adjusted by the wavelet representation. The reason is that wavelets correspond to filters with constant relative bandwidth $\frac{\Delta\omega}{\omega}$ [38].

3.3.2 Scale-Dependent Moments of Wavelet Coefficients

The temporal variation of the wavelet spectrum can be quantified by its standard deviation. Hence higher order moments of the wavelet coefficients \widetilde{S}_{ji} are necessary (see, e.g., [22, 23, 42]). The p th-order moment of the wavelet coefficients can be computed by summing up the p th power of the coefficients over all positions i ,

$$\widetilde{\mathcal{M}}_{p,j} = \frac{1}{2^j} \sum_{i=0}^{2^j-1} (\widetilde{S}_{ji})^p \quad (7)$$

The second-order moment is directly related to the scalogram via:

$$\widetilde{E}_j = 2^{j-1} \widetilde{\mathcal{M}}_{2,j}, \quad (8)$$

and the standard deviation of the scalogram at each scale 2^{-j} can then be defined as:

$$\sigma_{\widetilde{E}}(\omega_j) = \sqrt{\widetilde{\mathcal{M}}_{4,j} - (\widetilde{\mathcal{M}}_{2,j})^2} \quad (9)$$

Considering ratios of moments the scale-dependent flatness can be defined as:

$$\widetilde{\mathcal{F}}_j = \frac{\widetilde{\mathcal{M}}_{4,j}}{(\widetilde{\mathcal{M}}_{2,j})^2} \quad (10)$$

The relation between scale and frequency allows to express the flatness as function of the frequency ω_j , similarly to the wavelet spectrum. Note that Gaussian white noise, which is by definition non-intermittent, has a flatness equal to three for all frequencies.

Furthermore the scale-dependent flatness is related to the standard deviation of the spectral distribution by:

$$\widetilde{\mathcal{F}}_j = \left(\frac{\sigma_{\widetilde{E}}(\omega_j)}{\widetilde{E}(\omega_j)} \right)^2 + 1 \quad (11)$$

which shows that the flatness is a measure for the relative temporal fluctuation of the spectral energy density, as shown in [43] in the context of three-dimensional spatial energy spectra and applied to different turbulent flows.

3.4 Continuous Wavelet Cross-correlation

The continuous wavelet transform represents a time signal $s(t)$ in 2D wavelet space (time and scale) and is given by

$$\widetilde{s}(a, b) = \frac{1}{\sqrt{a}} \int_{-\infty}^{\infty} s(t) \psi^* \left(\frac{t-b}{a} \right) dt, \quad (12)$$

where $\psi(t)$ is the analyzing wavelet, a defines the scale and b defines the position in time of the wavelet. The symbol $*$ stands for complex conjugate. Then, the wavelet coefficient $\widetilde{s}(a, b)$ yields the contribution at time scale a of the signal $s(t)$ around the instant $t = b$. In the following we use the complex valued Morlet wavelet [44] given by $\psi(t) = \exp(-t^2/2\bar{\sigma}^2) \exp(2\pi i t)$, where $\bar{\sigma}$ defines the spectral

resolution of the wavelet ($\bar{\sigma} = 1$ gives the standard Morlet wavelet).

The cross-correlation of two signals s_1 and s_2 is defined as a normalized inner product of their wavelet transforms, as follows

$$C(a) = \frac{\int_{-\infty}^{\infty} \hat{s}_1(a, b) \hat{s}_2^*(a, b) db}{\left(\int_{-\infty}^{\infty} |\hat{s}_1(a, b)|^2 db \int_{-\infty}^{\infty} |\hat{s}_2(a, b)|^2 db \right)^{1/2}} \quad (13)$$

where \hat{s}_1 and \hat{s}_2 are the corresponding wavelet transforms. The cross-correlation function $C(a)$ is complex valued; its modulus shows the level of correlation of oscillations at a given scale (frequency) and takes values between zero and one. The phase of $C(a)$ indicates the mean phase shift of oscillations at a given scale. The wavelet cross-correlation was firstly introduced by [45] for the analysis of correlations of different characteristics of solar activity. In this study $\bar{\sigma} = 0.5$ is used to enhance temporal features.

To analyze and quantify the correlation of the two signals VSS and PIM at different scales we compute their wavelet cross-correlation. In Fig. 2 we plot the modulus of the wavelet cross-correlation function $|C(a)|$ as a function of scale a . It can be noticed that the correlation increases monotonically with scale, from values below 0.5 to values close to one for $a > 150$ min. This shows that all scales of the two signals are indeed correlated, but this correlation becomes weaker at finer scales.

3.5 Retrieving GIC by Orthogonal Wavelet Filtering

In the following we apply the wavelet-based method for extraction of coherent events out of magnetic signals, similar to what has been done in [22]. Each of the two signals $H_{VSS}(t)$ and $H_{PIM}(t)$ is thus decomposed as follows:

$$H_{VSS}(t) = H_{VSS}^C(t) + H_{VSS}^I(t) \quad (14)$$

and

$$H_{PIM}(t) = H_{PIM}^C(t) + H_{PIM}^I(t), \quad (15)$$

where the indices C and I correspond, respectively, to the coherent and incoherent parts of the signals. The incoherent contributions $H_{VSS}^I(t)$ and $H_{PIM}^I(t)$ correspond to the noise-like parts which are assumed to be uncorrelated and Gaussian.

In order to extract the GIC contribution, the coherent parts can be further split as follows:

$$H_{VSS}^C(t) = H^C(t) + H'_{VSS}(t), \quad (16)$$

and

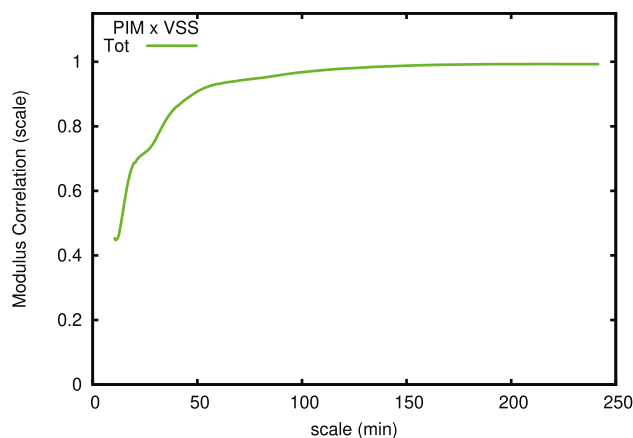


Fig. 2 Modulus of the wavelet cross-correlation function $C(a)$ for PIM and VSS signals, representing the correlation as a function of scale a

$$H_{PIM}^C(t) = H^C(t) + H'_{PIM}(t) + G(t). \quad (17)$$

where $H^C(t)$ denotes the magnetic effect of the outer contribution which can be considered to be the same for the two stations due to their relatively short distance. The local magnetic contributions of each station, denoted respectively $H'_{VSS}(t)$ and $H'_{PIM}(t)$ in the above formulas, can be considered to have a very slow time variation compared to the time scale of the experimental measurements, i.e., they exhibit a quasi-stationary behavior. The signal $H_{PIM}^C(t)$ contains in addition a non-negligible contribution, the geomagnetically induced current $G(t)$.

According to Eqs. 16 and 17, defining

$$\Delta H^C(t) = H_{PIM}^C(t) - H_{VSS}^C(t), \quad (18)$$

we have

$$\Delta H^C(t) = H'_{PIM}(t) - H'_{VSS}(t) + G(t), \quad (19)$$

which means that $\Delta H^C(t)$ can be decomposed into a low frequency contribution ($H'_{PIM}(t) - H'_{VSS}(t)$) and the contribution of the GICs. To recover the GIC we still need to eliminate the low frequency contribution. For this, we use a band-pass filter, which is now described.

The band-pass filtering procedure uses a moving average technique based on the orthogonal coordinate method, which has both a controlled performance and a well-known frequency response, adequate to avoid the introduction of spurious features in the signal retrieved. More details can be obtained in [46]. The highest frequency is determined from the data time resolution, as $\omega_{sup} = 8$ mHz, and the lowest one from the expected geophysical range [1], as $\omega_{inf} = 300$ μ Hz. The result of the band-pass filter applied to $\Delta H^C(t)$ yields the desired estimation for $G(t)$.

Once $G(t)$ is known, the GIC current itself can be estimated using Biot–Savart’s law:

$$G(t) = \mu_{air} \frac{I(t)}{2\pi r}, \tag{20}$$

where r is the radial distance of the magnetometer from the TL conductor ($r = 30$ m), and μ_{air} is the magnetic permeability of air, taken approximately as the magnetic permeability in vacuum, $\mu_0 = 1.2566 \times 10^{-6}$ m.kg.C⁻². This yields the following expression for the current expressed in Amperes:

$$I(t) = \frac{2\pi r}{\mu_0} G(t) \tag{21}$$

For experimental details we refer to [35].

The complete procedure for estimation of the GIC contribution is illustrated in Fig. 3. Instead of a direct calculation (left scheme) using the raw data from the station records, we use a non-linear wavelet filtering to extract first the coherent contributions from those signals and then compute the GIC (right scheme).

4 Results

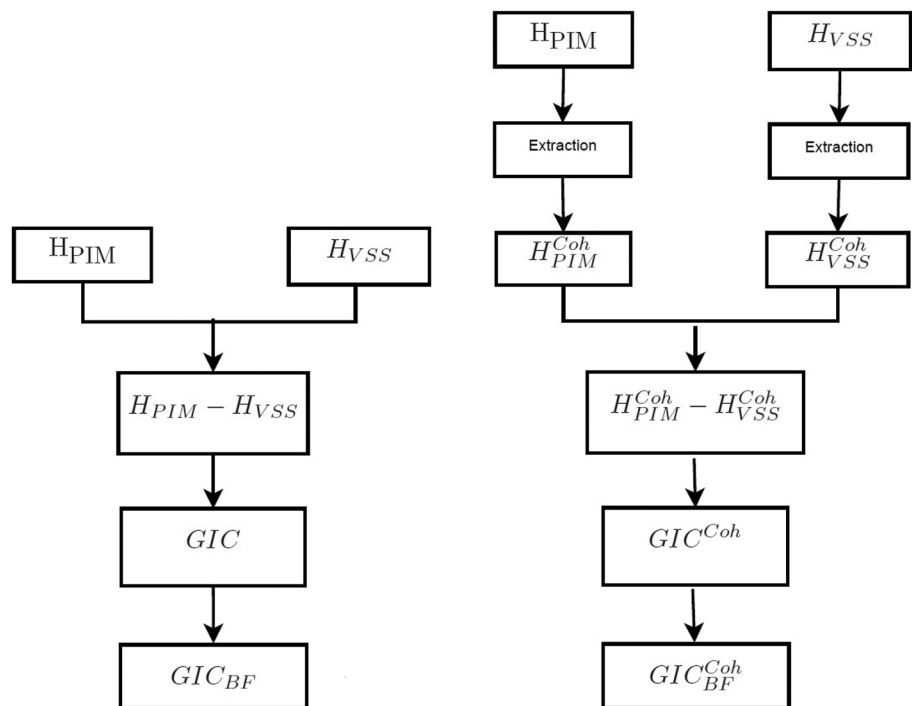
By the established wavelet-based analysis tool, the ground-recorded features of magnetospheric-ionospheric current effects at the Brazilian region are studied. After, a deperated GIC signal is retrieved.

4.1 Magnetospheric-Ionospheric Current Effects

By the numerical treatment, the two magnetic signals (Fig. 1) from the Pimenta-Barreiro site and the Vassouras observatory, are split into two orthogonal components: the coherent contributions and the incoherent ones, as shown in Fig. 4. The coherent (red) and incoherent (blue) contributions of Pimenta-Barreiro, denoted by PIM, are shown at the top of the figure (two superior panels). While the corresponding contributions for Vassouras (VSS) are shown at the bottom of the figure (two inferior panels). This procedure aids in distinguishing a clearer signal considering a white noise-affected signal. The coherent and incoherent contributions, which can be observed in the figure, exhibit completely different behaviour. The non-linear wavelet filtering disentangles the noisy (incoherent) contributions from the magnetic records on the surface, and the resulting coherent contributions motivate their use to identify an improved GIC.

The signal was first decomposed into an orthogonal wavelet basis, and the coherent contributions reconstructed from the wavelet coefficients whose modulus is larger than a threshold. The threshold value was recursively determined without any adjustable parameter. This algorithm is fast since it has linear complexity. The convergence of the iterative thresholding procedure for the denoising is illustrated in Fig. 5. We observe that the threshold rapidly converges towards the optimal value, i.e., after $n = 10$ iterations for PIM, and $n = 20$ one for VSS.

Fig. 3 Flowchart for computing the GIC. Direct calculation shown at left and wavelet-based calculation using the coherent contributions of the magnetic signals at right



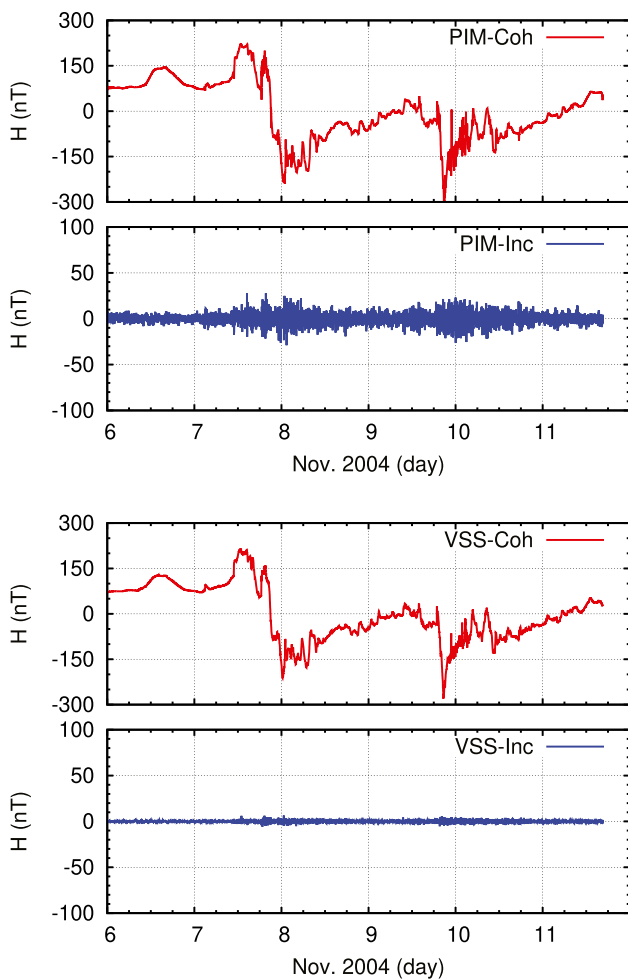


Fig. 4 Coherent and incoherent fluctuations split from the geomagnetic signal at Pimenta-Barreiro experimental site (top) and Vassouras observatory (bottom), during Nov. 06 to 11, 2004, corresponding to a data period of 5.6889 days

The statistical properties of the total signals and their coherent and incoherent components using the Coifman 12 orthogonal wavelet are summarized in the Table 1 for PIM and VSS. The number of wavelet coefficients, the minima and maxima

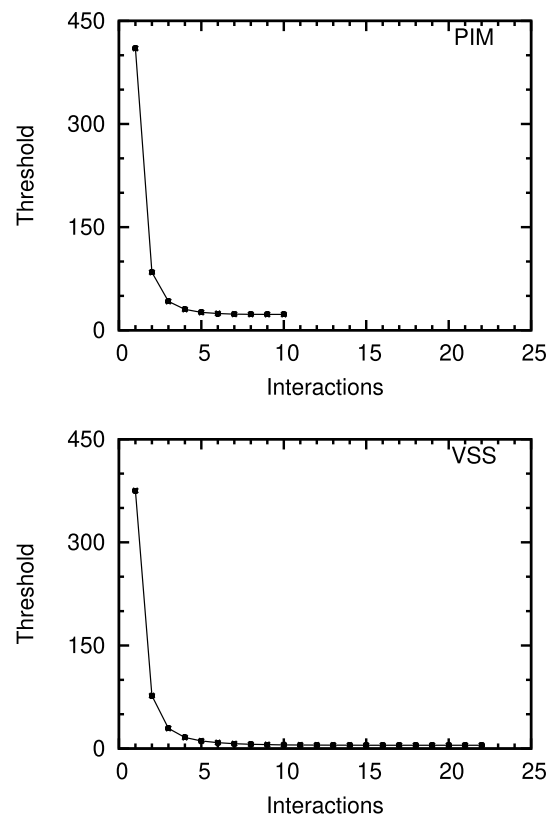


Fig. 5 Thresholding values versus iteration number for Pimenta-Barreiro (top) and Vassouras (bottom)

in the data of vanishing average, the variances σ^2 and their percentages, the ratio between signal and noise, and the skewness and flatness of signals are given. Figure 6 presents the percentage of coherent wavelet coefficient in each scale with respect to the total number of wavelet coefficient in that scale.

The coherent signals correspond to 4.5% and 11% of the wavelet coefficients and retain 99.69% and 99.98% of the total variance for PIM and VSS, respectively. In addition the extrema are well preserved. In contrast, the incoherent contributions $H(t)^I$ exhibit a different behavior. The 95.5% and 89% of the wavelet coefficients contribute only to 0.31% and 0.02%

Table 1 Statistical properties of the signal (S) and its coherent (S^C) and incoherent (S^I) components using the Coifman 12 orthogonal wavelet for PIM and VSS

Station Signal	PIM			VSS		
	S	S^C	S^I	S	S^C	S^I
# of coefficients	8192	368	7824	8192	880	7312
% of coefficients	100%	4.5%	95.5%	100%	11 %	89 %
min H (nT)	-323	-321	-29	-279	-280	-5.8
max H (nT)	247	222	28	215	214	6
Variance σ^2	9330	9301	29	7813	7812	1
% of variance	100 %	99.69 %	0.31 %	100 %	99.98 %	0.02 %
Sig/Noise (dB)	—	25	—	—	38	—
Skewness	-0.04	-0.04	0.01	0.09	0.09	0.07
Flatness	10	31	4.5	15	29	5.3

of the total variance for PIM and VSS, respectively. The resulting signal-to-noise ratios are $SNR = 10 \log_{10}(\sigma^2/\sigma_{Inc}^2) = 25$ dB, for PIM, and 38 dB, for VSS.

For both stations the skewness of the incoherent contribution is almost zero and the flatness has values close to three, which confirms that this contribution is indeed noise like with quasi-Gaussian statistics. The total and coherent signals of both stations have flatness values larger than three, indicating the presence of intermittency. In both cases the skewness values are close to zero.

The probability density functions (PDF), shown in Fig. 7, of the total signal H and the coherent and incoherent contributions are presented in semi-logarithmic coordinates in figure for PIM and VSS. The PDFs are estimated using histograms with 25 bins and the integrals are normalized to one.

For both PIM and VSS the PDFs of the total and coherent signal have a quasi-Gaussian shape with the absolute skewness values less than 0.09, as seen in Table 1. In both cases the PDF of the incoherent component is symmetric and close to a Gaussian shape (cf. insets of Fig. 7) which is in accordance with their skewness 0.00 and flatness 3.00.

Figure 8 shows the Fourier and wavelet spectra for the total signal H (green), the coherent component H^C (red), and the incoherent component H^I (blue) for PIM. Figure 9 presents a similar analysis for VSS. In both cases we observe that the wavelet spectrum superimposes to the Fourier spectrum without exhibiting oscillations, which confirms that the former is a consistent estimator. The modified periodograms (not shown here) would yield similar smoothed estimators like wavelet spectra, as discussed in [22].

For both signals we observe that the spectra of the total and coherent parts are very similar, except that for Vassouras an enhanced decay is observed for higher frequencies. For intermediate frequencies in the interval $10^{-3.7}$ and 10^{-2} the spectra exhibit a power law scaling ω^α with $\alpha \simeq -5/3$, which indicates long range correlation since the spectral slope is negative. In contrast, the incoherent components have in both cases a flat spectrum, corresponding to energy equipartition which shows that these components are indeed decorrelated.

To analyze the intermittency of the signal and its different contributions, we plot the flatness $\tilde{F}(\omega_j)$ versus frequency ω_j in Fig. 10. Note that the signal reconstructed from its wavelet coefficients at a given scale j corresponds to the band-pass

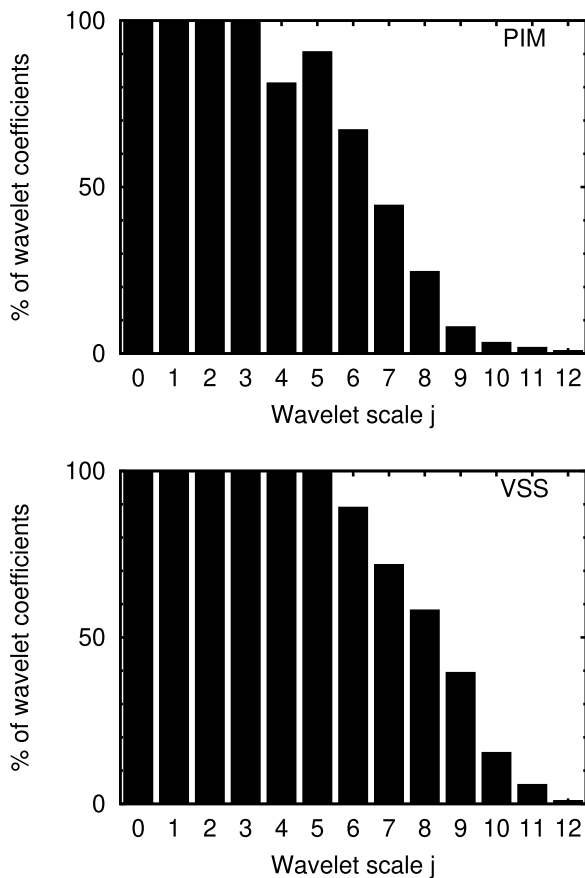


Fig. 6 Number of wavelet coefficients versus scale for Pimenta-Barreiro (top) and Vassouras (bottom)

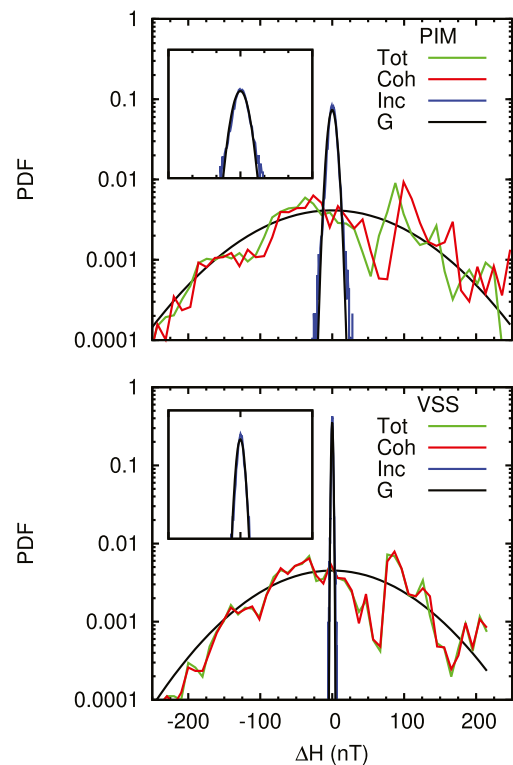


Fig. 7 Probability density function of the total signal (green), the coherent component (red), and the incoherent component (blue), together with Gaussian fits for Pimenta-Barreiro (top) and Vassouras (bottom). ΔH represents the variation related to the mean values of the datasets. The insets show a zoom of the incoherent component where each x-tic is 25 nT

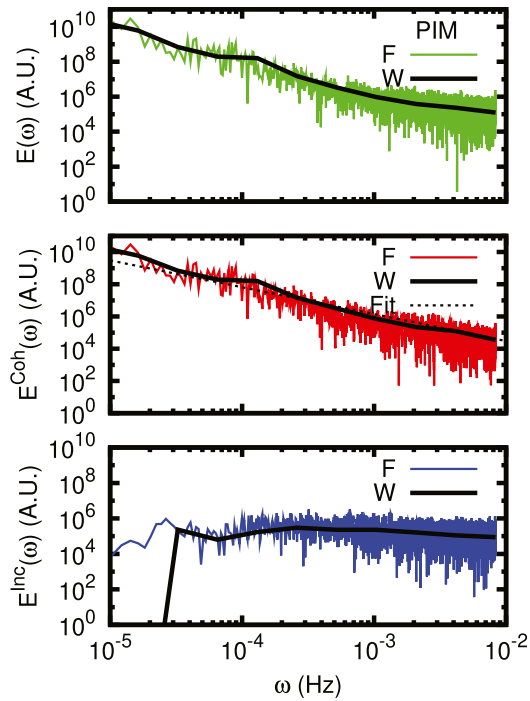


Fig. 8 Fourier (color) and wavelet (black) spectra of the total signal $dH(t)$ (top), the coherent component dH^C (middle) and the incoherent component dH^I (bottom) for Pimenta-Barreiro. The fit (black dotted line for the coherent contribution) shows ω^α with $\alpha = -5/3$

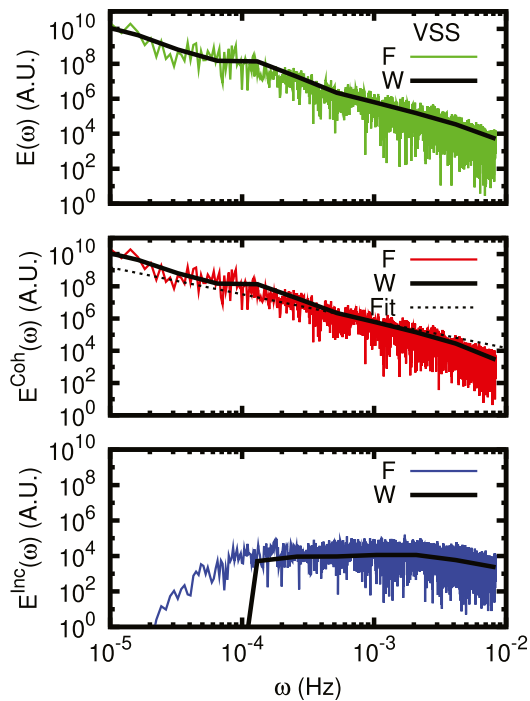


Fig. 9 Fourier (color) and wavelet (black) spectra of the total signal $dH(t)$ (top), the coherent component dH^C (middle) and the incoherent component dH^I (bottom) for Vassouras. The fit (black dotted line for the coherent contribution) shows ω^α with $\alpha = -5/3$

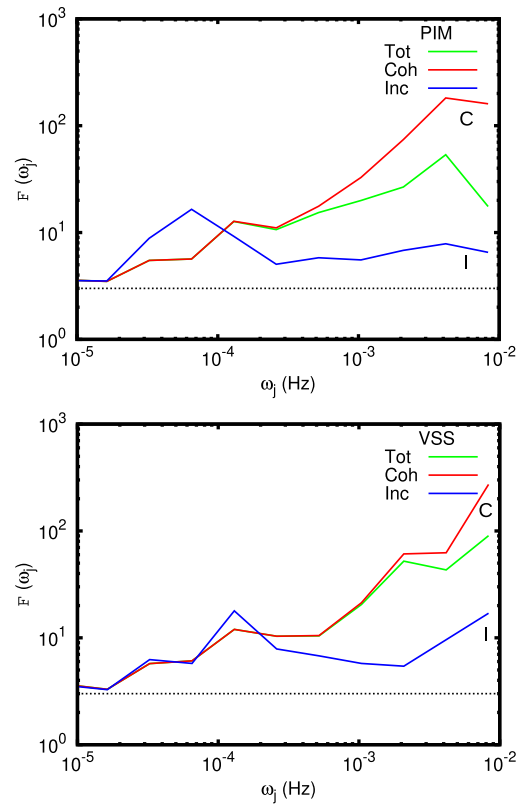


Fig. 10 Flatness \mathcal{F} versus frequency ω_j (in Hz) of the total signal (red), the coherent contribution (green) and the incoherent contribution (blue) for Pimenta-Barreiro (top) and Vassouras (bottom). The value $\mathcal{F}_t = 3$ corresponds to the Gaussian behavior

filtered signal around the frequency $\omega_j = \omega_\psi / 2^j$. The value $\mathcal{F}_t = 3$ corresponding to the flatness of a Gaussian process is also indicated. For both the total signal and the coherent contribution the flatness increases with increasing frequency and the values for the coherent part (> 100) are above of the one of the total part. This indicates that the coherent contribution is even more intermittent than the total signal. In contrast, the flatness of the incoherent contribution does not show such a strong increase and yields much smaller values (< 20) which gives evidence for a less intermittent behavior. Nevertheless a departure from the value $\mathcal{F}_j = 3$ is observed, which shows that the incoherent part is not perfectly Gaussian.

The wavelet energy spectra (continuous lines) together with the standard deviation of the temporal fluctuations of energy (line with markers) are shown for the total, coherent and incoherent parts in Fig. 11 for PIM (top) and VSS (bottom). We observe that all curves of the total and coherent signals perfectly superimpose. The incoherent parts show much smaller fluctuations and are hence less intermittent, as already illustrated for the scale-dependent flatness, which are directly related using Equation 11.

To complete the statistical analyses, the characterization of the correlation between the total, coherent and incoherent contributions, the modulus of the wavelet cross-correlation function is shown in Fig. 12 for PIM and VSS. For PIM and VSS we find a pronounced correlation between the total and coherent parts, i.e., $|C(a)| > 0.8$ and $|C(a)| > 0.95$, respectively. The correlation between the total and incoherent parts is much weaker, i.e., $|C(a)| < 0.6$ and $|C(a)| < 0.6$ for PIM and VSS, respectively. Finally, as expected, the correlation between the coherent and incoherent parts are much smaller ($R < 0.2$) for all scales.

4.2 Extraction and Analysis of the GIC Signal

Once the coherent contributions of the horizontal components of geomagnetic fields measured on the ground have been extracted, the GIC contribution can be obtained using the procedure explained in Sect. 3.5. The estimation of the current induced in the TL is appropriately obtained using Biot-Savart’s law (Eq. 21). The result is shown in Fig. 13 and allows an easy comparison among the different procedures.

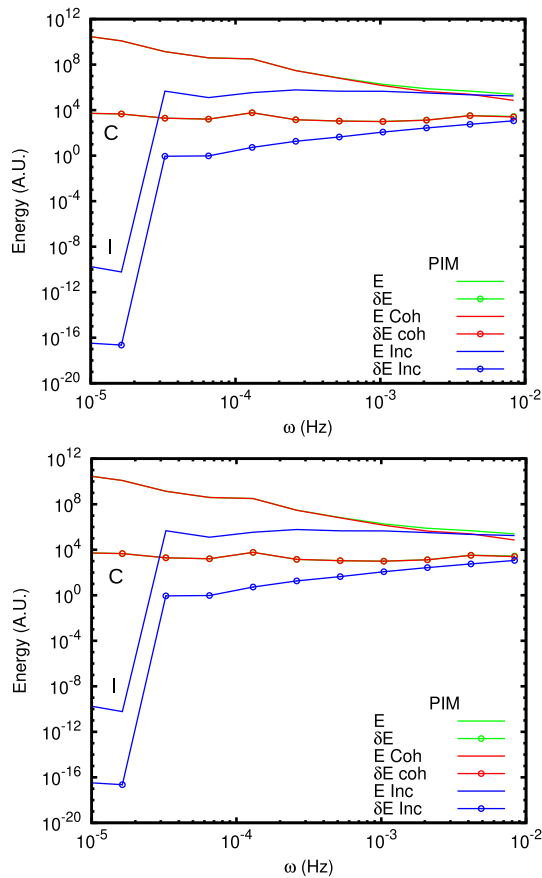


Fig. 11 Wavelet energy spectrum E (line) and corresponding standard deviation E (marked line) versus frequency ω_j (in Hz) for the total (green), coherent (red) and incoherent (blue) signals for Pimenta-Barreiro (top) and Vassouras (bottom)

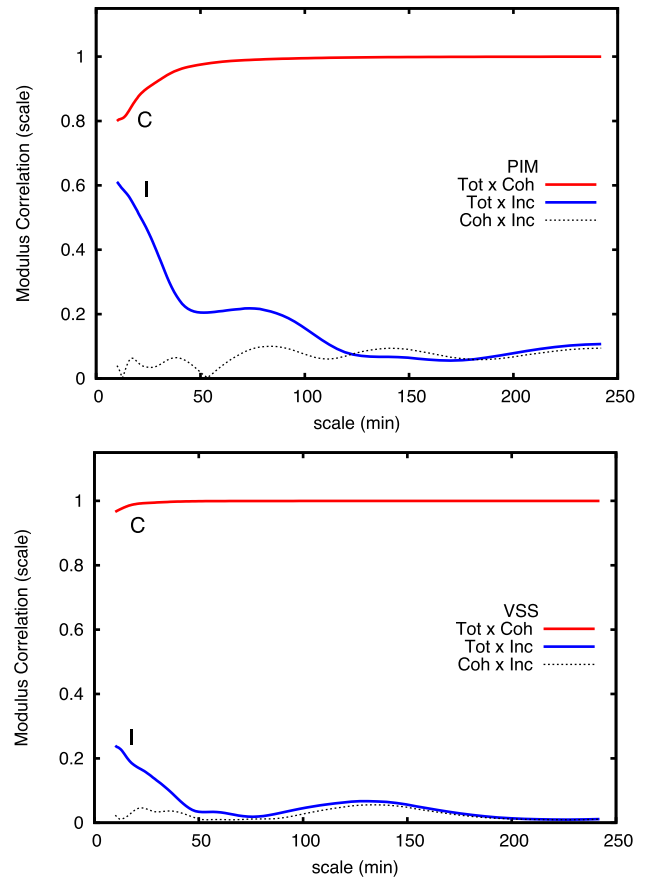


Fig. 12 Modulus of the wavelet cross-correlation function $|C(a)|$ between total, coherent and incoherent signals for PIM (top) and VSS signals (bottom) as a function of scale a

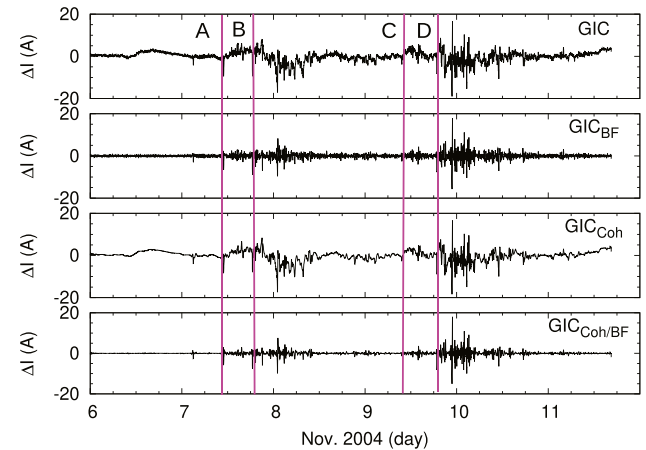


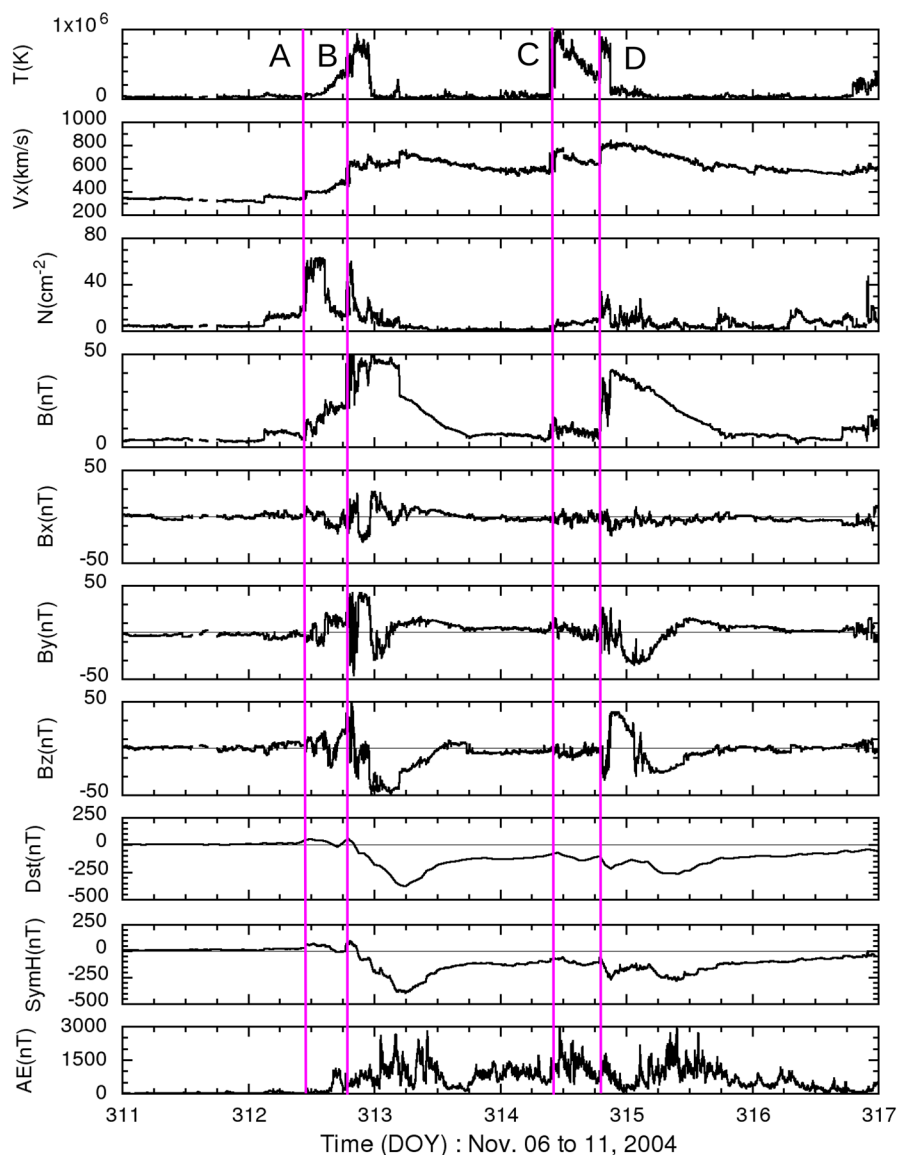
Fig. 13 Respectively from top to bottom, (i) the raw GIC obtained by the difference between the magnetic records from Pimenta-Barreiro experimental site and Vassouras observatory, (ii) band-pass filtered GIC using moving average with the Gaussian ordinate method, (iii) GIC retrieved from the coherent contributions using the orthogonal wavelet denoising method applied to the data of both stations, and (iv) the former treated by the band-pass filter. Vertical lines refer to moments of sudden magnetopause current increase

At the top of the figure, the panel presents the GIC obtained directly by the difference between the magnetic records from Pimenta-Barreiro experimental site and the Vassouras Observatory. It represents a raw result. In the second panel, taking into account a band-pass filtering using a moving average with the Gaussian ordinate method, in order to avoid generating spurious frequencies, a better result can be obtained. However, noise is evident in the signal, and it disturbs a good identification of the GIC event. In the third panel, dealing with coherent contributions using the orthogonal wavelet denoising method applied to the data of both stations, one can obtain a clearer signal. At the bottom panel, by the same band-pass filtering, a well-identified GIC event is finally established.

All the procedures implemented in this paper compose a complete methodology of analysis and identification of GIC events. It establishes an objective tool that allows a GIC analysis implementation in an automatic computational basis.

At last, helped by the depured signal presented at the bottom panel in the figure, we can interpret a physical interaction between the interplanetary behaviour and the GIC occurrence. The comparison of Figs. 14 and 13 highlights that the GIC start (about 12:00h on 7 Nov) coincides with the sudden commencement (line A). Line B indicates an intensification of GIC related to a sudden geomagnetic impulse and magnetopause compression (increasing the magnetopause current). Line C displays an intensification of GIC related to another sudden magnetopause compression, and line D refers to a significant GIC increase associated with another magnetopause compression. The signal treatment result presented here allows, beyond highlighting the GIC for occurrences measured in the electrodynamically disturbed South American region, endorsing the primary cause of GIC at low latitudes, such as comprehensively discussed in [32–34]. As magnetic measurements are far from

Fig. 14 Space environment parameter conditions which affected the Earth geomagnetically on November 06-11, 2004, which the Temperature T , radial speed V_x , density N of the solar plasma, the Interplanetary Magnetic Field components (B_x , B_y , B_z , in GSM reference system) and magnitude B , and the geomagnetic indices: equatorial Dst , symmetric $SymH$, and Auroral electrojet AE are shown. Vertical lines indicate beginning of a magnetopause compression



the equatorial electrojet influence, this work has identified a clear contribution related to the sudden increase of the magnetopause current, concerning periods of the magnetopause compression occurring together with geomagnetic storm occurrences.

5 Conclusions

Motivated by a laboratory analysis on tokamak current fluxes, we have presented a similar study on the effects of natural electric currents from the magnetospheric-ionospheric system, using magnetic datasets collected under well-controlled experimental conditions in a Brazilian region close to the South Atlantic Magnetic Anomaly.

As methodology an algorithm based on the orthogonal wavelet transform, considered an optimal technique for denoising signals corrupted with additive Gaussian white noise was applied to the magnetic records on the ground. The signal was first decomposed into an orthogonal wavelet basis, and the coherent contributions reconstructed from the wavelet coefficients whose modulus is larger than a threshold. The threshold value is recursively determined without any adjustable parameter. This algorithm is fast since it has linear complexity. With this non-linear multiscale filtering technique, the incoherent part of the signal could be removed. So, the coherent part retrieved as a signal could be used to study the GIC phenomena better than the raw signal or one filtered under stationarity assumptions.

We have shown that the flatness of the coherent contributions increases faster for higher frequencies than that one of the total signal. This result shows that the coherent signal is more intermittent than the raw data. In contrast, the flatness of the incoherent contribution indicates it with a non-intermittent behavior. Note that contrary to the results obtained by [22], the PDFs of the coherent contributions in this study case show a more Gaussian shape than a skewed shape. This feature could be due to a balance in energy distribution about a mean value of the natural current, with intermittent events occurring symmetrically on both sides (related to the evolution of the geomagnetic storms).

Using the Fourier spectrum superimposed to the wavelet spectrum, the scale-dependent behavior analyses (represented as energy per frequency) have shown that the energy contributions decrease from the lower frequencies to the higher ones according to a power law and a slope of $-5/3$ which is typical in turbulent processes.

Thus, at last, besides the result of a cleaner GIC reached for this case study, this work has developed and characterized a methodology to retrieve potentially GIC events from an ensemble of magnetometers under a fast, easy and confident experimental procedure.

As future perspectives, for the South America investigations, diagnoses on some features of the space electrodynamic interactions between the solar plasma and magnetosphere-ionosphere that produce magnetic effects on the surface could be addressed with the statistical analyses using the Fourier-Wavelet filtering methodology presented here.

Appendix

Interplanetary Conditions

Figure 14 shows the space environment parameter conditions which affected the Earth geomagnetically on November 06-11 (or Day Of Year 311 to 316), 2004. At the top panels, T is the temperature, V_x radial speed V_x , N numerical density of the plasma solar wind, B_x , B_y , B_z the components (in GSM reference system) and B the magnitude of the Interplanetary Magnetic Field. While, at the bottom panels, the equatorial Dst , symmetric $SymH$, and Auroral electrojet AE (in nanoteslas) are the geomagnetic disturbance indices shown.

Concisely, about the middle of 07 November (DOY 312), a fast speed plasma stream ($V_x > 600$ km/s), incident upon a slow speed stream (≈ 300 km/s), reached the Earth's location producing the occurrence of a higher plasma density and IMF fluctuations. Later about the middle of 09 November (DOY 314), another fast stream episode occurred, triggering magnetic reconnection again. Nevertheless, details of the interplanetary parameters seem to show characteristics of interplanetary magnetic clouds [6] appearing at about 21:00h on 07 November and 18:00h on 09 November. Sinusoidal fluctuations in the B_z or B_y components identify those kinds of interplanetary phenomena (MC). They are preceded sequentially by a significant increase in the density, a shock (characterised by parameter discontinuities), and a sheath with a rise in the temperature. In the own MC, the density and temperature typically decrease. The southward B_z component (< -5 nT) was responsible for triggering a magnetic reconnection (a merging between the IMF and the geomagnetic field), a condition which produced a very intense geomagnetic disturbance ($Dst = -374$ nT and $AE > 1000$ nT) recorded on the ground magnetometers. Those electrodynamic causes are connected to the geomagnetically induced currents analysed in this study.

In the figure, the Dst indicates a sudden storm commencement at about 12:00h on 7 November, followed by the main phase of the geomagnetic storm with a peak ($Dst = -374$ nT) at about 06:00h on 8 November (local time 03:00h), ruled essentially by the southward B_z component. Later, in the recovery phase, by a new intensification of the southward B_z , a low-latitude geomagnetic decrease occurs (a secondary peak, $Dst = -250$ nT) about 21:00h on 09

November (local time 18:00h). During this geomagnetic storm interval, there are magnetopause compression episodes, noticed easier when the density and speed present simultaneously sudden increases in the magnitude. In the analysis, we use the Dst or Sym-H instead of AE because the formers properly concern low-latitude geomagnetic effects, as our data of GIC represent that. In the figure, the vertical lines (designated as A, B, C, and D), as examples, identify abrupt increases in the magnetopause compression, which trigger increases in the magnetopause current.

Acknowledgements This work was supported by grants from CNPq (424352/2018-4, 307083/2017-9, and 306985/2021-7), and FAPESP (2020/13015-0). M.D., M.F. and K.S. thank the ANR (project “M2TFP”) and K.S. (project SiCOMHD) for financial support. M.D. and O.M. and K.S. thank the Institut Carnot STAR, Marseille, for financial support. M.D. thanks école Centrale de Marseille and CNRS, department S2TI. MF, NNVY and KS acknowledge support by the French Federation for Magnetic Fusion Studies (FR-FCM) and of the Eurofusion consortium from the Euratom research and training programme 2014–2018 and 2019–2022 under grant agreement No 633053. The views and opinions expressed herein do not necessarily reflect those of the European Commission. The authors thank Dr. Icaro Vitorello (im memorian) and the engineering staff of FURNAS Centrais Eletricas S.A, Rio de Janeiro, RJ, Brazil for the data. O.M., M.D. and M.F. thank the Wissenschaftskolleg zu Berlin and CIRM/CEMRACS-Marseille, France, for its kind hospitality. The authors thank Dr Ari Viljanen for providing Finnish magnetometer datasets gently. We are grateful to V. E. Menconni for their helpful computational assistance. The authors thank all free(dom)-software and opensource teams, mainly GNU/Octave and gnuplot ones. An earlier work [2] used the magnetometer data to study the relationship with the interplanetary parameter B_z (found in http://plutao.sid.inpe.br/col/dpi.inpe.br/plutao/2010/11.11.16.27/doc/Mendes_GIC.pdf). Data are available from the international repositories (World Data Center-C, Tokyo: <https://wdc.kugi.kyoto-u.ac.jp/wdc/Sec3.html>; and OMNI Web Service, NASA: https://omniweb.gsfc.nasa.gov/form/omni_min.html) and from INPE by request.

Author Contribution All authors cooperate with expertise in the same proportion in the work.

Funding OM and MOD received grants from CNPq (424352/2018-4, 307083/2017-9, and 306985/2021-7), FAPESP (2020/13015-0), and CEA/EURATOM n° V.3258.001. MF, NNVY and KS from the French Federation for Magnetic Fusion Studies (FR-FCM) and of the Eurofusion consortium from the Euratom research and training programme 2014–2018 and 2019–2022 under grant agreement No 633053.

Availability of Data and Materials Data are available from the international repositories (World Data Center-C, Tokyo; and OMNI Web Service, NASA) and from INPE by request.

Code Availability Codes are available from free(dom) software or specific part demanding to the corresponding author.

Declarations

Ethics Approval The work followed better human and scientific practices.

Consent to Participate All participants consent to the work.

Consent for Publication All participants consent for publication.

Conflict of Interest The authors declare no competing interests.

References

1. W.H. Campbell, Introduction to Geomagnetic Fields, p. 337. Cambridge University, Cambridge (2003). <https://doi.org/10.1017/CBO9781139165136>
2. O. Mendes, M.O. Domingues, N.B. Trivedi, GIC-occurrences analysis: a case study. Proceedings of the 9th Brazilian Conference on Dynamics Control and their Applications DINCON **10**, 850–855 (2010)
3. D.M. Oliveira, C.M. Ngwira, Geomagnetically Induced Currents: principles. Braz. J. Phys. **47**(5), 552–560 (2017). <https://doi.org/10.1007/s13538-017-0523-y>
4. R. Pirjola, V. Bothmer, I.A. Daglis, Space weather effects on power grids. In: Bothmer, V., Daglis, I.A. (eds.) Space Weather - Physics and Effects, pp. 269–288. Springer, Berlin (2007). https://doi.org/10.1007/978-3-540-34578-7_10
5. I.A. Daglis, (ed.), Effects of Space Weather on Technology Infrastructure. NATO Sciences, vol. 176. Kluwer Academics, Amsterdam (2004)
6. C.T. Russell, J.G. Luhmann, R.J. Strangeway, Space Physics An Introduction. Cambridge University, Cambridge (2016)
7. A. Pulkkinen, E. Bernabeu, J. Eichner, C. Beggan, A.W.P. Thomsom, Generation of 100-year geomagnetically induced current scenarios. Space Weather **10**, 04003 (2012). <https://doi.org/10.1029/2011SW000750>
8. E.O. Falayi, O. Ogunmodimu, O.S. Bolaji, J.D. Ayanda, O.S. Ojoniyi, Investigation of geomagnetic induced current at high latitude during the storm-time variation. NRIAG J. Astron. Geophys. **6**(1), 131–140 (2017). <https://doi.org/10.1016/j.nrjag.2017.04.010>
9. A.C. Kellerman, R. Mcgranaghan, J. Bortnik, B.A. Carter, J. Hughes, R.F. Arritt, K. Venkataramani, C.H. Perry, J. McCormick, C.M. Ngwira, M. Cohen, J. Yue, Geomagnetically induced currents at middle latitudes: 1. quiet-time variability. Space Weather **20**(2) (2021). <https://doi.org/10.1029/2021SW002729>
10. T. Kikuchi, Y. Ebihara, K. Hashimoto, K. Kitamura, S. Watna, Reproducibility of the geomagnetic induced currents at middle latitudes during space weather disturbances. Front. Astron. Space Sci. **11**, 759431 (2021). <http://doi.org/10.3389/fspas.2021.759431>
11. T. Divett, D.H. Mac Manus, G.S. Richardson, C.D. Beggan, C.J. Rodger, M. Ingham, E. Clarke, A.W.P. Thomson, M. Dalzell, Y. Obana, Geomagnetically induced current model validation from New Zealand’s South Island. Space Weather **18**(8), 2020–002494 (2020). <https://doi.org/10.1029/2020SW002494>
12. A. Pulkkinen, A. Viljanen, K. Pajunpää, R. Prijola, Recordings and occurrence of geomagnetically induced currents in the Finnish natural gas pipeline network. J. Appl. Geophys. **48**(4), 219–231 (2001). [https://doi.org/10.1016/S0926-9851\(01\)00108-2](https://doi.org/10.1016/S0926-9851(01)00108-2)
13. M. Svanda, A. Smicková, T. Vybostoková, Modelling of geomagnetically induced currents in the Czech transmission grid. Earth, Planets and Space **73**(229), 1–11 (2021). <https://doi.org/10.1186/s40623-021-01555-5>
14. A. Pulkkinen, R. Kataoka, S. Watari, M. Ichiki, Modeling geomagnetically induced currents in Hokkaido Japan. Adv. Space Res. **46**(9), 1087–1093 (2010). <https://doi.org/10.1016/j.asr.2010.05.024>

15. R. Pirjola, 2. In: Mosquera Cuesta, H.J. (ed.) Geomagnetically induced currents as ground effects of Space Weather, pp. 28–44. Intechopen, London (2012). <https://doi.org/10.5772/29840>
16. J.K. Hargreaves, The Solar-terrestrial Environment. Cambridge Atmospheric and Space Science, vol. 5, p. 420. Cambridge University, Cambridge (1995)
17. C. Barbosa, L. Alves, R. Caraballo, G.A. Hartmann, A.R.R. Papa, Analysis of geomagnetically induced currents at a low-latitude region over the solar cycles 23 and 24: comparison measurements and calculations. *J. Space Weather. Space Clim.* **5**(A25) (2015). <https://doi.org/10.1051/swsc/2015036>
18. L.R. Alves, C. Barbosa, R. Caraballo, G.A. Hartman, A.R.R. Papa, R. Pirjola, Geomagnetically induced currents measured in Brazil: 5 years of monitoring during solar cycle 24. *Latinmag Letters* **6**(A01), 1–5 (2016). Special Issue
19. K.V. Espinosa, A.L. Padilha, L.R. Alves, Effects of ionospheric conductivity and ground conductance on geomagnetically induced currents during geomagnetic storms: case studies at low-latitude and equatorial regions. *Space Weather* **17**(2), 252–268 (2019). <https://doi.org/10.1029/2018SW002094>
20. N.B. Trivedi, I. Vitorello, W. Kabata, M.B. Pádua, S.L.G. Dutra, A.L. Padilha, M.S. Bologna, M.J.F. Barbosa, A.P. Soares, G.S. Luz, F. Abreu Pinto, Effects of geomagnetically induced currents-gic on electric power technology in Brazil. Eleventh International Congress of the Brazilian Geophysical Society, SEG Global Meeting Abstracts, 66–69 (2009). <https://doi.org/10.1190/sbgf2009-017>
21. S. Mallat, A Wavelet Tour of Signal Processing. Academic Press, Burlington (1998). <https://doi.org/10.1016/B978-0-12-374370-1.X0001-8>
22. M. Farge, K. Schneider, P. Devynck, Extraction of coherent bursts from turbulent edge plasma in magnetic fusion devices using orthogonal wavelets. *Phys. Plasmas* **13**(2006). <https://doi.org/10.1063/1.2172350>
23. M. Farge, K. Schneider, Wavelet transforms and their applications to MHD and plasma turbulence: a review. *J. Plasma Phys.* **81**(6) (2015). <https://doi.org/10.1017/S0022377815001075>
24. D. Donoho, I. Johnstone, Ideal spatial adaptation via wavelet shrinkage. *Biometrika* **81**(3), 425–455 (1994). <https://doi.org/10.1093/biomet/81.3.425>
25. A. Viljanen, A. Koistinen, K. Papjunpää, R. Pirjola, P. Posio, A. Pulkkinen, Recordings of geomagnetically induced currents in the Finnish natural gas pipeline - summary of an 11-year period. *Geophysica* **46**(1–2), 59–67 (2010)
26. V. Bothmer, I.A. Daglis, (eds.): *Space Weather, Physics and Effects.*, p. 127. Springer, Chichester (2007)
27. G.K. Parks, *Physics of Space Plasmas, An Introduction.* Westview, Colorado (2004)
28. M.G. Kivelson, C.T. Russel, (eds.): *Introduction to Space Physics*, p. 568. Cambridge University, Cambridge (1995)
29. W.D. Gonzalez, B.T. Tsurutani, A.L. Clúa de Gonzalez, Interplanetary origin of geomagnetic storms. *Space Science Reviews* **88**(3/4), 592–562 (1999). <https://doi.org/10.1023/A:1005160129098>
30. W.D. Gonzalez, J.A. Joselyn, Y. Kamide, H.W. Kroehl, G. Rostoker, B.T. Tsurutani, V.M. Vasyliunas, What is a geomagnetic storm? *J. Geophys. Res.* **99**(A4), 5771–5792 (1994). <https://doi.org/10.1029/93JA02867>
31. N.B. Trivedi, I. Vitorello, W. Kabata, S.L.G. Dutra, A.L. Padilha, M.S. Bologna, M.B. Pádua, A. PinhelSoares, G.L. Sarcinelli, R. Pirjola, A. Viljanen, Geomagnetically induced currents in an electric power transmission system at low latitudes in Brazil: a case study. *Space Weather* **5**, 04004 (2007). <https://doi.org/10.1029/2006SW000282>
32. R.A.D. Fiori, D.H. Boteler, D.M. Gillies, Assessment of GIC risk due to geomagnetic sudden commencements and identification of the current systems responsible. *Space Weather* **12**(1), 76–91 (2014). <https://doi.org/10.1002/2013SW000967>
33. B.A. Carter, E. Yizengaw, R. Pradipta, A.J. Halford, R. Norman, K. Zhang, Interplanetary shocks and the resulting geomagnetically induced currents at the equator. *Geophys. Res. Lett.* **42**(16), 6554–6559 (2015). <https://doi.org/10.1002/2015GL065060>
34. D.M. Oliveira, D. Arel, J. Raeder, E. Zesta, C.M. Ngwira, B.A. Carter, E. Yizengaw, A.J. Halford, B.T. Tsurutani, J.W. Gjerloev, Geomagnetically induced currents caused by interplanetary shocks with different impact angles and speeds. *Space Weather* **16**(6), 636–647 (2018). <https://doi.org/10.1029/2018SW001880>
35. W. Kabata, I. Vitorello, M. Banik, N.B. Trivedi, W.C. Cunha, Magnetômetros fluxgates amorfos robustos para pesquisa em sondagens magnéticas profundas no brasil. *Revista de Física Aplicada e Instrumentação* **17**(3), 99–109 (2004)
36. A. Mendes da Costa, M.O. Domingues, O. Mendes, C.G.M. Brum, Interplanetary medium condition effects in the South Atlantic Magnetic Anomaly: A case study. *J. Atmos. Sol. Terr. Phys.* **73**(11/12), 1478–1491 (2011). <https://doi.org/10.1016/j.jastp.2011.01.010>
37. O. Mendes, M.O. Domingues, A. Mendesda Costa, A.L. Clúade Gonzalez, Wavelet analysis applied to magnetograms: Singularity detections related to geomagnetic storms. *J. Atmos. Sol. Terr. Phys.* **67**, 1827–1836 (2005). <https://doi.org/10.1016/j.jastp.2005.07.004>. [SPECIAL ISSUE]
38. I. Daubechies, *Ten Lectures on Wavelets.* Series in Applied Mathematics, vol. 61. (SIAM), Philadelphia, PA, Pennsylvania (1992)
39. M. Farge, K. Schneider, N. Kevlahan, Non-Gaussianity and coherent vortex simulation for two-dimensional turbulence using adaptive orthonormal wavelet basis. *Phys. Fluids* **11**(8), 2187–2201 (1999). <https://doi.org/10.1063/1.870080>
40. A. Azzalini, M. Farge, K. Schneider, Nonlinear wavelet thresholding: a recursive method to determine the optimal threshold value. *Appl. Comput. Harmon. Anal.* **18**(2), 177–185 (2005). <https://doi.org/10.1016/J.ACHA.2004.10.001>
41. M.B. Priestley, *Spectral Analysis and Time Series.* Academic, New York (1981)
42. K. Schneider, M. Farge, N. Kevlahan, Spatial intermittency in two-dimensional turbulence: a wavelet approach. In: Tongring, N., Penner, R.C. (eds.) *Woods Hole Mathematics, Perspectives in Mathematics and Physics.* Series on knots and everything, vol. 34, pp. 302–328. World Scientific, Singapore (2004). https://doi.org/10.1142/9789812701398_0007
43. W.J.T. Bos, L. Liechtenstein, K. Schneider, Small scale intermittency in anisotropic turbulence. *Phys. Rev. E* **76**(2007). <https://doi.org/10.1103/PhysRevE.76.046310>
44. A. Grossmann, J. Morlet, Decomposition of Hardy functions into square integrable wavelets of constant shape. *SIAM J. Math. Anal.* **15**(4), 723–736 (1984). <https://doi.org/10.1137/0515056>
45. E. Nesme-Ribes, P. Frick, D. Sokoloff, V. Zakharov, J. Ribes, A. Vigourous, F. Laclare, Wavelet analysis of Maunder minimum as recorded in solar diameter data. *Comptes Rendus de l'Academie des Sciences* **321**(12), 525–532 (1995). ISSN: 1251-8069
46. O. Mendes, A. Mendesda Costa, F.C.P. Bertoni, Effects of the number of stations and time resolution on Dst derivation. *J. Atmos. Sol. Terr. Phys.* **68**(18), 2127–2137 (2006). <https://doi.org/10.1016/j.jastp.2006.01.015>

Publisher's Note Springer Nature remains neutral with regard to jurisdictional claims in published maps and institutional affiliations.

Springer Nature or its licensor holds exclusive rights to this article under a publishing agreement with the author(s) or other rightsholder(s); author self-archiving of the accepted manuscript version of this article is solely governed by the terms of such publishing agreement and applicable law.